Formation of electric-field domains in a system of multiple finite superlattices

M. Hosoda and S. Noma
Department of Applied Physics, Osaka City University, Sugimoto, Sumiyoshi-ku, Osaka 558-8585, Japan
(Received 16 November 2006; revised manuscript received 29 March 2007; published 23 May 2007)

We report the formation of an electric-field domain in a multiple finite-superlattice (MFSL) system in which finite superlattices are separated by thick barriers. Our experimental results show that even though the MFSL system has no negative-differential-resistance region in the current-voltage characteristics, the system exhibits electric-field domain formation. This phenomenon can be explained by our simulation of the inner electric-field distribution, taking into account transport and the concentration of carriers in the MFSL. We found that Fowler-Nordheim tunneling in a thick barrier is a key factor in generating the inhomogeneous space-charge distribution that forms electric-field domains.

DOI: 10.1103/PhysRevB.75.205333 PACS number(s): 73.50.Fq, 73.21.Cd, 73.40.Gk, 73.63.Hs

I. INTRODUCTION

Since the discovery of electric-field domain (EFD) formation in semiconductor superlattices (SLs) by Esaki and Chang,[1] the phenomenon has attracted much attention and study.[2,3] Until now, the EFD has been investigated for simple-structured SLs that consist of the same quantum wells (QWs) and barriers throughout the entire SL periods. In these systems, the EFD is caused by an inhomogeneous carrier distribution due to intersubband resonances, e.g., resonance between the ground and first excited subbands.[2,3]

In this paper, we report an EFD in a multiple finite-superlattice (MFSL) system in which finite-superlattices (FSLs) are separated by thick barriers (TBs). Even though the system had no negative-differential-resistance (NDR) region caused by subband resonances, the system showed an EFD. The characteristics of the EFD formation are analyzed from the experimental results, and the origin is confirmed by a numerical simulation.

II. EXPERIMENTS AND SAMPLE STRUCTURE

The sample structure we used is shown in Fig. 1. The sample was constructed from multiple FSLs separated by thick barriers. The samples were grown on (100)-oriented n^+-GaAs substrates by molecular beam epitaxy; the growth sequence was an n^+-GaAs buffer layer, an n-$Al_{0.3}Ga_{0.7}As$ clad layer, a 50-nm $Al_{0.3}Ga_{0.7}As$ undoped cladding layer, undoped MFSL, a 50-nm $Al_{0.3}Ga_{0.7}As$ undoped cladding layer, a p-$Al_{0.3}Ga_{0.7}As$ clad layer, and a p^+-GaAs cap. Each FSL was constructed from five periods of GaAs/$Al_{0.3}Ga_{0.7}As$ multiple QWs, with GaAs QW widths of 17 monolayers (ML) and AlGaAs barrier widths of 8 ML, with 25-nm $Al_{0.3}Ga_{0.7}As$ undoped TBs on both ends.

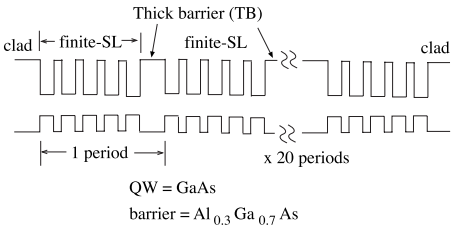

FIG. 1. Schematic figure of undoped region in the p-i-n diode sample. The multiple finite superlattices (finite SLs) are separated by thick barriers (TBs). Each finite SL is constructed from 5 periods of 17-monolayer (ML) GaAs QW with an 8-ML $Al_{0.3}Ga_{0.7}As$ barrier. The undoped area in the p-i-n diode is composed of 20-period finite SL and TB with two cladding layers of 50-nm $Al_{0.3}Ga_{0.7}As$ in both ends.

The sample was fabricated into p-i-n diode mesas of 400- or 50-μm squares. Alloyed Au electrodes were prepared to apply the electric field to the intrinsic region, and the Ohmic contact was confirmed by examining the forward-biased current-voltage characteristics. The built-in voltage corresponding to the flatband condition was about 1.5 V of the forward-bias voltage for all samples. In this report, forward bias is denoted with a "−" sign, the reverse direction of the bias is written as "+" voltage, and thus the flatband condition is denoted by −1.5 V.

A 633-nm cw HeNe laser was used as the excitation source. Carrier density in the p-i-n structure was controlled by the excitation power. The excitation light was injected from the p-cap side and focused by a 10× objective lens. Photoluminescence (PL) from the sample was also collected by the same objective lens. The spot diameter of the excitation light was approximately 30 μm. Under this condition, the estimated density of the photogenerated carriers in the sample was in the order of 10^{11} cm^{-2} under a 1-mW excitation intensity. All data were measured at 20 K. Here, we show experimental results from 400-μm square mesa samples unless otherwise noted.

III. EXPERIMENTAL RESULTS

A. Photocurrent-voltage characteristics

Evidence of EFD formation is observed in the photocurrent-voltage characteristics (I-V curve). Figure 2 shows the I-V curve. From the I-V curve demonstrated under weak excitation, we found that there is no NDR region. The photocurrent monotonically increases as the reverse-bias voltage increases. In contrast, under strong excitation, the I-V curve shows steplike oscillation. This is evidence of an EFD as previously reported.[1–3] The number of oscillations is about 20, which agrees with the number of FSLs in the

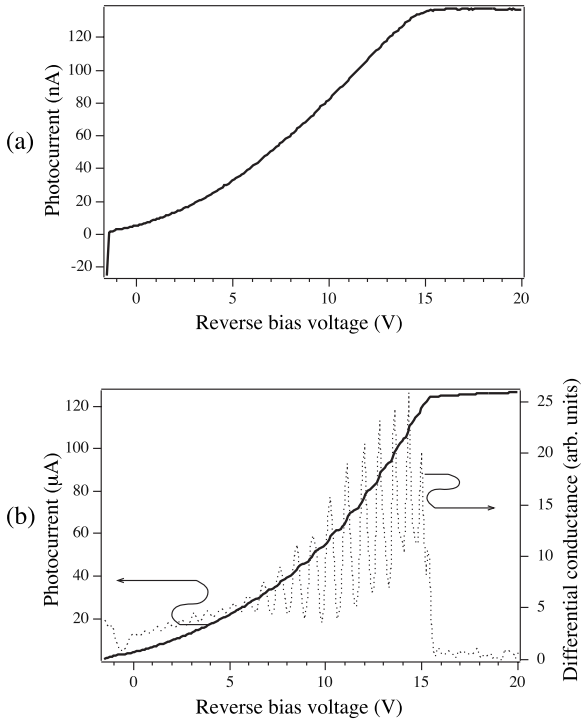

FIG. 2. Photocurrent versus reverse bias voltage characteristics (I-V curve) under 10-μW (a) and 1-mW (b) HeNe laser excitation. The dotted line is the differential conductance.

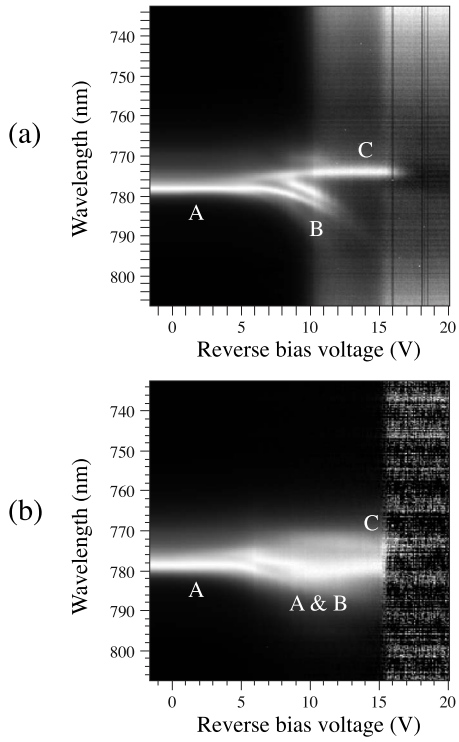

FIG. 3. Normalized PL spectra as a function of reverse-bias voltage under 10-μW (a) and 1-mW (b) HeNe laser excitation. The normalization is done to the highest PL peak at each voltage. Brightness (gray level) represents PL intensity. The white area corresponds to high PL intensity.

MFSL (cf. Fig. 1). However, the oscillation is not sawtooth in shape, as has been observed in conventional superlattices,[2,3] but steplike in structure. The origin of this characteristic is analyzed in later sections.

B. Photoluminescence characteristics

Figure 3 shows the PL spectra as a function of the reverse-bias voltage. The observed PL wavelengths corresponding to the intersubband transitions described below agree well with our calculated values for the sample structure, for which we took into account ±1 of monolayer fluctuation, slight deviation of Al contents in the AlGaAs layers at growth, and exciton binding energy up to 10 meV. The miniband width ΔE evaluated from the 10-μW PL spectra is approximately 30 meV, which is slightly smaller than the calculated value for the 17/8 ML FSL. We conclude that this arises from the monolayer fluctuation and the difference in Al contents in the barrier.

Since the FSL has thin and low barriers (8-ML $Al_{0.3}Ga_{0.7}As$), a miniband is formed in the FSL under zero along with a very weak electric field. The PL spectra under weak excitation in Fig. 3(a) can be explained by the radiative recombination processes shown below. The PL branch A in Fig. 3 is emission from the miniband bottoms in the FSLs. Branch B is emission from a −1 Stark ladder.[4,5] Branch C is emission from localized subband states in isolated QWs. In conventional SLs with thin barriers, radiative recombination shows the following behavior with an increasing electric field. Under the flatband condition or a very weak electric field, a miniband is formed and radiative recombination occurs between the miniband bottom and the ground heavy-hole state. This transition energy is lower than that of the intrinsic subband energy in isolated QWs. The energy difference is $\frac{1}{2}\Delta E$, where ΔE is the miniband width.[4,5] As the applied electric field increases, the miniband vanishes and the electron wave function localizes in one QW; then, a subband is formed. Consequently, PL is emitted from the subband and the transition energy increases. Under an intermediate electric field between the miniband and subband formations, a Stark-ladder state[4,5] is generated and radiative recombination occurs simultaneously with the Stark ladder. Ordinarily, emission from a lower-energy ladder state—i.e., the −1 Stark ladder—is dominant.[4]

The electric field F necessary to break the miniband is $\frac{1}{2}\Delta E = eFD$, where e is the unit charge, F is the electric field, and D is the SL period.[4,5] Therefore, in our sample, localization should occur at about 1-V reverse-bias voltage. This critical voltage is less than that observed in Fig. 3(a), about 12 V. This indicates screening of the local electric field in the FSL region. Other electric fields are applied to the TB region by way of compensation to the total applied voltage of the sample. Therefore, even under weak excitation, many carriers remain in the FSLs due to blocking of carrier transport by TBs and the electric field in FSLs is less than that in TBs due to a space-charge field screening. As the reverse-bias voltage becomes sufficiently high, the field screening is broken; then, the miniband finally vanishes and the PL branches B and C appear alternately to branch A. Although for investigating the field screening it would be preferable to

obtain additional PL spectra under further weak excitation, we could not obtain clear PL spectra throughout the entire voltage range under weaker excitation intensity than 10 μW due to the poor signal-to-noise ratio.

Although PL branch *B* shows a clear energy change of the −1 Stark ladder, it appears to be a doublet. This is thought to originate from a nonuniform field distribution in the MFSL. In fact, we found a nonuniform electric-field distribution and some field screening in our simulation results even at 10-μW excitation, which will be described later.

Under the high-excitation condition exemplified in Fig. 3(b), branches *A* and *B* (indicated by *A* and *B* in the figure) exist in a wide voltage range—i.e., about 5–15 V—and a weak branch *C* appears simultaneously from 8 to 15 V. This coexistence of the three PL branches indicates an inhomogeneous electric-field distribution in the MFSL. Therefore, the origin of the oscillation in the *I*-*V* curve under the 1-mW excitation in Fig. 2(b) is thought to be related to the above electric-field distribution—i.e., the formation of an EFD. The coexistence of the PL branches is interpreted as follows: under the bias voltage region exhibiting the EFD formation, three conditions of the electric field in FSLs coexist in the MFSL. One is FSLs having a miniband positioned in a low electric-field domain (LFD), which experience a weak local electric field. A second is FSLs having a localized subband in a high electric-field domain (HFD), which experience a large electric field. The other is a FSL-generating Stark-ladder PL at the domain boundary between the LFD and HFD, which suffers a transition in field strength from low to high as the domain moves in the MFSL.

The origin of the smeared PL branch *B* in Fig. 3(b) compared to that in Fig. 3(a) is thought to be the overlap of weak Stark-ladder PL branches at each bias voltage that is generated from a single FSL. Only a single FSL at the EFD boundary can emit Stark-ladder PL during the movement of the domain boundary. On the other hand, under the weak excitation shown in Fig. 3(a), the PL branch of the Stark ladder is generated from all FSLs in the MFSL. Therefore, its intensity is high and the spectrum is clear. Also, the other PL branches are clear and do not coexist in a wide voltage range. The above observations indicate that all FSLs in MFSL systems suffer the same electric field under a low carrier density, and thus the nonexistence of an EFD is confirmed from this PL behavior.

The weak intensity of PL branch *C* under the high-excitation condition originates from the quenching phenomenon. Promotion of the carrier sweep-out from FSLs under a high electric field in the HFD region decreases the rate of radiative recombination. Therefore, branch *C* is weaker than the other PL branches that are emitted from FSLs placed in the LFD region. We should note that the intensity of PL branch *C* under the weak excitation condition in Fig. 3(a) is seen as a strong PL; however, its intensity is very weak. The PL intensity was normalized by the PL peak at each voltage. The comparison of the PL intensity is correct only when multiple PL branches coexist at a particular voltage. The absolute PL intensity is discussed in Sec. III D.

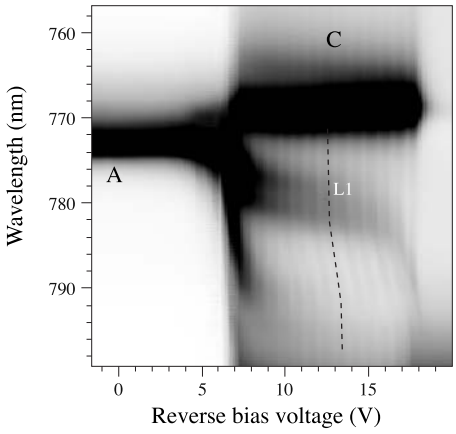

FIG. 4. Normalized PL spectra of a 50-μm mesa sample as a function of reverse-bias voltage under 0.1-mW HeNe laser excitation. The normalization is done to the highest PL peak at each voltage. Gray level (not brightness) represents PL intensity; i.e., the black area corresponds to high intensity. The dashed line guides a Stark-ladder branch (*L*1).

C. Movement of domain boundary observed by photoluminescence

Clear separation of the Stark-ladder PL during movement of the domain boundary can be observed by using 50-μm square mesa samples. Figure 4 shows normalized PL spectra from a 50-μm square mesa sample under 0.1-mW excitation. The gray level shows PL intensity with the black area representing a higher PL intensity. *L*1 is PL from a −1 Stark ladder, the gradient of which indicates the transition of the local electric field in a FSL. There are approximately 15 teeth of a comblike structure constructed from the L1 PL branches. (We draw only one *L*1 line to clearly display the image in Fig. 4.) Since the gradient of the *L*1 branch is steep, the change in the local electric field in a FSL is very rapid during the movement of the EFD boundary, as will be proved by our simulation in Sec. V C. Kinks in the *L*1 line indicate that the transition of the local electric field in a FSL varies by two or three electric field strengths with a movement of the domain boundary. We could not identify the origin of the relatively high-PL-intensity area at around a 780-nm wavelength and in the 8–17-V voltage range. This might come from an increase in the overlap integral between the wave functions, such as the Franz-Keldysh effect.[6,7]

The PL structure indicates the transition of electric field intensity in an individual FSL. Since the domain boundary between the LFD and HFD moves through the MFSL, individual FSLs at the domain boundary experience low to high electric fields. This transition of the electric field generates a Stark-ladder PL, and thus about 15 comb teeth arise in the PL image. However, the number of teeth is less than the 20 periods of FSLs in the MFSL. The reason may be that some teeth overlapped within the fat branch at around 7–8 V in the beginning of the EFD formation.

We have not been able to observe the above fine PL structure from 400-μm square mesa samples. This may be due to the spatially lateral diffusion of photocarriers in QWs. Since the beam spot size of the excitation laser is 30 μm, lateral

diffusion is sufficiently strong under the high excitation condition in the 400-μm square mesa samples. This generates spatially inhomogeneous distribution of the carrier density in a QW or FSL, thus also generating spatially inhomogeneous electric field screening, which smears the EFD formation and its PL spectra. For 50-μm square mesa samples, since the spot size is of the same order, the influence of the lateral diffusion is weak; i.e., the lateral carrier distribution is relatively homogeneous. In fact, we have observed a clear oscillation structure in an *I-V* curve from a 50-μm square sample under a 0.1-mW excitation, whose intensity is less than the 1 mW needed for a 400-μm square mesa sample. In an excitation condition higher than 0.1 mW, the comb structure was smeared due to broadening of the spectral peak width of the Stark-ladder PLs.

We should note that the comblike fine structure in the PL has not been reported in the study of EFD formation in conventional superlattice systems. Our direct observation of the individual movement of the domain boundary using the PL measurement can be considered rare. The reason for this success is that the emission wavelength of the Stark-ladder PL is very sensitive to the local electric field. Therefore, by using the observation of the Stark-ladder PL, the transition of the local electric field can be clearly observed. On the other hand, in conventional SLs, since the EFD formation needs relatively thick barriers, PL from the Stark ladder is very weak and thus difficult to observe. This is the reason that our observation is a rare one. In addition, our finding illustrates that the mesa size versus the excitation spot size is also a key feature for observing the fine structure.

D. Accumulation of carriers in FSLs

Accumulation of space charge is the origin of the EFD formation, which generates vertically inhomogeneous electric-field distribution due to space-charge electric-field screening. To investigate the accumulation, PL intensity and photocurrent are useful for estimating the degree of carrier transport. These values are complementary in high-quality semiconductors having low nonradiative recombination. The decrease in the PL intensity due to the promotion of carrier transport and the subsequent increase in output current has been commonly known as quenching. Figure 5 shows voltage dependences of the PL intensity integrated over the whole PL wavelength region and that of the photocurrent. Under weak excitation, where an EFD is not established, the PL intensity decreases rapidly as the photocurrent increases and vanishes at about 10 V. On the contrary, under high excitation, the PL does not vanish at 10 V but sustains a considerable intensity up to 15 V. Within this voltage range, the *I-V* curve shows a clear oscillation that indicates EFD formation. This sustained PL implies a residual carrier accumulation in the FSL region, in which accumulated carriers screen the electric field and cause the EFD formation.

IV. MODEL OF ELECTRIC-FIELD DOMAIN FORMATION IN MFSL DERIVED FROM EXPERIMENTAL RESULTS

From the experimental results described so far, we can create a model of EFD formation in the MFSL. Figure 6 shows the model. In the FSLs, carrier transport is very effective due to miniband transport under a low electric field and nonresonant sequential tunneling through the thin barriers under a high electric field. In contrast, the efficiency of the carrier transport across the multiple FSLs is significantly small due to lower tunneling efficiency to the TBs. Since the carriers can move smoothly in the FSLs, electrons gather in the rightmost QW next to the TBs. The holes also gather in the leftmost QW in a FSL. Since there is no or very low carrier density in the TBs, an electric field is dominantly applied to the TB area. The effective transport of carriers through the TBs is accomplished by Fowler-Nordheim tunneling for the triangle-shaped barrier formed under a high electric field. The concentration of carriers in the QWs on both sides of the TBs generates a high electric field, and the field is applied to the TB area, which promotes the escape of carriers from the FSLs by Fowler-Nordheim tunneling, as shown in Fig. 6. Once a FSL enters a HFD regime, shown as region *C* in Fig. 6, blocking of the carrier transport by the TB is released. The domain boundary exists at a TB that is sandwiched between the *B*-FSL and the next FSL in region *C*. The electric field applied to the TB at the domain boundary increases with an increase in the external applied bias voltage to the MFSL. Increasing the bias voltage further slants the electric potential in the TB up to the same potential gradient in region *C*. Simultaneously, carriers trapped in FSL *B*

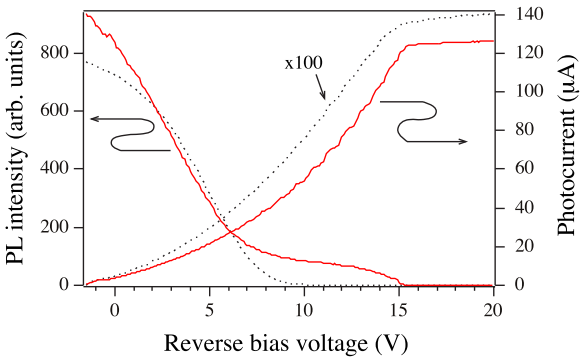

FIG. 5. (Color online) Integrated PL intensity (two curves marked by left-hand curved arrow) and *I-V* curve (two curves marked by right-hand curved arrow) as a function of reverse bias voltage under 10-μW (black dotted lines) and 1-mW (red solid lines) HeNe laser excitation. Photocurrent under 10-μW excitation is multiplied by 100.

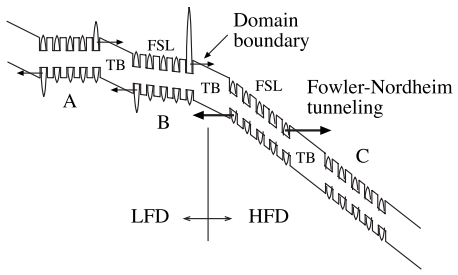

FIG. 6. Schematic figure for the model of EFD and carrier transport from FSLs through thick barriers. Parabolic curves indicate carrier concentration in QWs; that is, upper (inverse parabola) and lower curves indicate electron and hole concentrations, respectively.

are permitted to escape by Fowler-Nordheim tunneling. This escape reduces the space-charge screening in FSL *B*, and finally the potential gradient in FSL *B* becomes equivalent to that in region *C*.

Under an electric field, a charge separation between electrons and holes occurs, caused by their opposite directions of transfer. This carrier separation to the opposite ends of a FSL generates screening of the inner electric field in the FSLs in region *A* in Fig. 6. The screening makes the electric field flat or low and generates a LFD region.

The model of the EFD is highly consistent with the experimental results. The coexistence of the three PL branches in Figs. 3(b) and 4 is assigned as PL emission from regions *A* to *C* in Fig. 6. The sustained PL intensity under the EFD formation regime in Fig. 5 originates from the PL emission from FSLs in the LFD region as well as from a FSL at the domain boundary in Fig. 6. The oscillation in the *I*-*V* curve can be interpreted as a flash flooding of concentrated carriers in a QW left next to a TB at a domain boundary, as shown in Fig. 6. The movement of the domain boundary changes the efficiency of the Fowler-Nordheim tunneling of the TB due to the variation in the electric potential gradient.

Regarding low excitation intensity, the model can also explain the PL behavior in Fig. 3(a). Since the efficiency of the carrier transport is different in the FSL and TB regions, carriers are also blocked by the TBs even under low carrier density, and they screen the electric field in the FSLs as in region *A* in Fig. 6. The long-lived PL emission from the miniband's bottom in Fig. 3(a) indicates that the electric field in FSLs is screened and that most of the electric field is applied to the TBs. When the reverse-bias voltage increases, the potential gradient in the TBs increases, the efficiency of the Fowler-Nordheim tunneling increases, and the blockage of carrier transport is broken. Since the carrier density is insufficient to generate an EFD, all FSLs suffer from the same electric field and the transition of the PL spectra is identical in all FSLs, as shown in Fig. 3(a).

V. VERIFICATION OF THE ELECTRIC-FIELD DOMAIN BY SIMULATION

A. Velocity of carrier transport in MFSL

To calculate the local electric field, carrier distribution has to be determined. Since the distribution is calculated from the movement of the carriers, determining carrier velocity as a function of the electric field is necessary. Since the carrier velocity is the reciprocal of tunneling time, the tunneling time has to be determined.

Figure 7 shows four cases of tunneling conditions. In the case of Fig. 7(a), tunneling probability is

$$T = \exp\left[-\frac{2L_b\sqrt{2m_b^* H_{b0}}}{\hbar}\right], \tag{1}$$

where the L_b, m_b^*, and H_{b0} are the barrier length, the effective mass in the barrier, and the effective barrier height, respectively.[8] For cases (b) and (c), the WKB approximation (Wentzel-Kramers-Brillouin method) is used[9,10]:

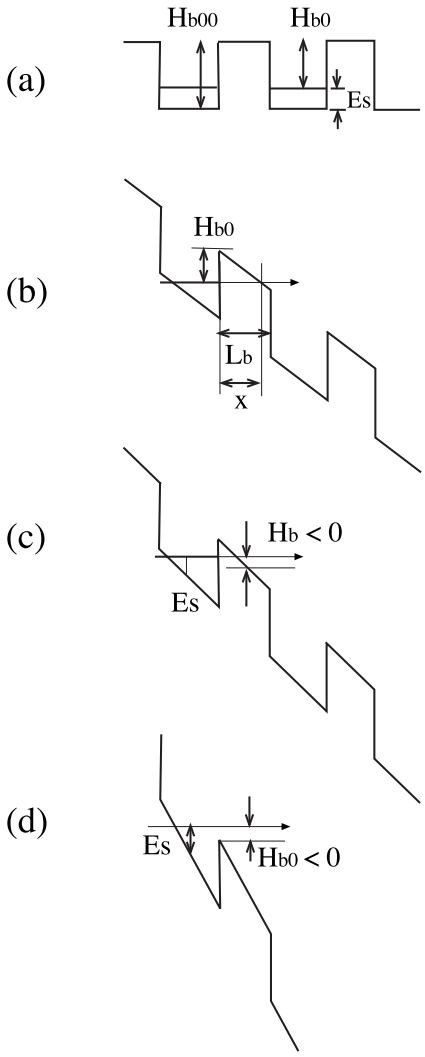

FIG. 7. Various tunneling conditions. Hb, Lb, and Es are barrier height, barrier thickness, and subband energy, respectively.

$$T = \exp\left[-\frac{2}{\hbar}\int_{x_1}^{x_2}\sqrt{2m(V(x)-E)}dx\right], \tag{2}$$

where $V(x)$ and E are an arbitrary barrier potential and particle energy, respectively. (x_1, x_2) is an interval where $V(x) \geq E$. Then, for case (b), where $x \geq L_b$ and $x = \frac{H_{b0}}{eF}$,

$$T = \exp\left[-\frac{4\sqrt{2m_b^*}}{3eF\hbar}[(H_{b0}-eFL_b)^{3/2} - H_{b0}^{3/2}]\right], \tag{3}$$

where e and F are unit charge and electric field, respectively. For case (c), where $x \leq L_b$, the same WKB equation is also valid and gives

$$T = \exp\left[-\frac{2}{\hbar}\int_0^{H_{b0}/eF}\sqrt{2m_b^*(H_{b0}-eFx)}dx\right]$$
$$= \exp\left[-\frac{4\sqrt{2m_b^*}}{3eF\hbar}H_{b0}^{3/2}\right]. \tag{4}$$

For case (d), the calculation and estimation of the carrier transport encounters difficulty, since the term in the square root in Eq. (2) becomes negative. In addition, since the carriers enter into the continuum, the carriers run there for a while and then are retrapped into the other QWs. The calculation and evaluation of this multiple process is complex. Fortunately, our experimental condition and its local electric field in the sample do not meet such a high-electric-field area. Therefore, we neglected it and saturated the maximum carrier velocity by the maximum value calculated in case (c).

In regard to a low electric field near zero, Eq. (1) has a discrepancy that results in a large nonzero velocity v_0 even under a zero electric field, approximately 10^8 cm/s in the FSL region, which does not fit with the reality of real-space carrier transport. This discrepancy comes from a model that only treats the tunneling of a wave function, where the electron wave alternately goes to and returns from a QW and the barrier areas when the electric field is zero. To overcome this discrepancy, we replaced velocity v_0, derived from Eq. (1) under a near-zero electric field, with velocity $v_g=\mu F$, derived from carrier mobility μ under a region of the electric field F where $v_0 \geq v_g$. This procedure is important for taking into account the carrier velocity between QWs in the FSL region. Although we used the above replacement for the TB area too, this approximation did not sufficiently influence our simulation results, since the key factor in the EFD generation depends on the quality of the tunneling efficiency through the TBs *under a relatively high electric field*. For velocity passing through the TB, there is a strong electric field dependence at a higher-electric-field region rather than at a near-zero-field region, and this characteristic makes a significant contribution to forming the EFD as described later.

Miniband transport in FSLs was also considered, and we replaced its velocity v_m with v_g. Since v_m is also too large even under a zero electric field—i.e., approximately 5×10^7 cm/s for a 30-meV miniband width in our sample—we believe that it does not express real-space transport under a zero electric field. In addition, minibands with a small band width easily vanish under a weak electric field, a phenomenon known as the Wannier-Stark localization (WSL). Miniband transport is then replaced by nonresonant sequential tunneling using Eq. (3) after the localization.[11] Although such localization frequently generates NDR in the *I-V* curve,[12,13] we neglected this possibility since we could not observe any NDR in the *I-V* curve. In addition, since the miniband width of our sample is relatively small, we assume that the difference in the electron velocity between the miniband transport and the nonresonant sequential tunneling is small. In fact, this conclusion is supported by the small current output and the absence of the NDR under very low bias voltages in Fig. 2. The NDR by the WSL appears at a very-low-bias-voltage region near the flatband condition. Therefore, if anything, the NDR should be observed in the *I-V* curve from −1.5 V (flatband condition in the *p-i-n* diode) to the 0-V bias voltage range, for example. However, there is no NDR in the experimental *I-V* curve in Fig. 2(a). We also conclude that this absence of the NDR results from the TBs sandwiching the FSLs, which strongly obstructs carrier transport between the FSLs. In contrast to electron transport, we did not consider minibands for hole transport, since the miniband width is significantly small due to its heavy effective mass.

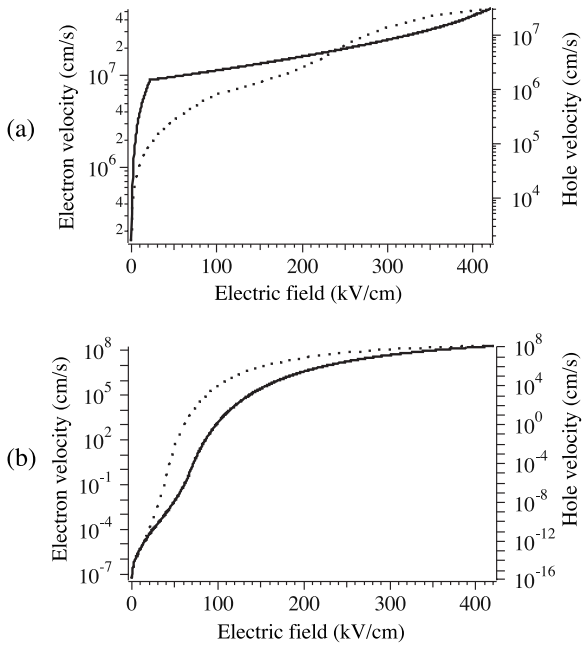

FIG. 8. Electron (solid line) and heavy-hole (dotted line) velocity in FSL (a) and for TB (b) as a function of electric field.

Figure 8 shows calculated carrier velocities as functions of the electric field. Values used for the calculation are as follows: electron subband energy from the GaAs QW conduction-band bottom=81 meV for 17-ML single QW, heavy-hole (hh) subband energy from GaAs QW valence-band bottom=24 meV, electron mobility=8500 cm^2/V, and hh mobility=450 cm^2/V.[14,15] Other material constants are typical values,[14] and the temperature is 20 K. The important characteristic of the velocity curves is that the tunneling velocity for a TB in a low-electric-field region is very slow for both electrons and holes. This means that some characteristic of TBs blocks the escape of carriers from FSLs under a low-electric-field regime. However, the velocity becomes very fast from about 200 kV/cm due to the effective Fowler-Nordheim tunneling under the steep gradient of the electric potential in the TB and its low barrier height (Al content is 0.3).

The blocking of carriers by the TBs generates an accumulation of carriers in the QWs in the FSLs beneath the TBs. It then weakens the inner electric field in the FSLs due to field screening and instead increases the potential gradient in the TBs, as shown in Fig. 6. In contrast, the calculated carrier velocity in the FSLs is considerably fast, especially for holes, even under low electric fields due to the thin barriers in the FSL region and their low barrier height. Therefore, carriers can freely move in a FSL. Then, it is easy to establish the charge separation between the electrons and holes caused by the opposite transfer direction to the electrons and holes under an electric field. This carrier separation accumulates carriers next to the TBs, which promotes field screening in the FSLs. These differences in carrier transports for the FSL and TB regions are the origin of the EFD formation. Once inhomogeneous field distribution arises under a high carrier den-

sity, the above process is accelerated by nonlinear dynamics due to nonlinear velocity curves as well as the field screening. This in turn establishes a stable EFD in the MFSL.

B. Calculation method

The calculation method of the EFD formation is as follows: As a first step, photogenerated carriers are injected into the MFSL with a carrier distribution calculated from an absorption coefficient of 10 000 cm^{-1} for a 633-nm HeNe laser. The laser light is injected from the *p*-cap side—that is, from the left side of Figs. 1 and 6. The spot diameter of the irradiation is assumed to be 40 μm, which is similar to the experimental condition.

Second step: the electric potential is calculated from the carrier distribution by using a classical one-dimensional Green function[16] due to the symmetry of the QW systems. We used this integral-type equation since numerical solutions of the differential equation—i.e., the Poisson equation—sometimes result in instability in simulations of nonlinear dynamics. We chose a one-dimensional coordinate z with boundary conditions at 0 and L. This system can be solved as a Dirichlet problem.[16] The Green function representing a unit charge at position ζ is

$$G(z|\zeta) = \begin{cases} \frac{1}{L}z(L-\zeta), & z < \zeta, \\ \frac{1}{L}\zeta(L-z), & z > \zeta. \end{cases} \tag{5}$$

The electric potential when there is a carrier density of $\rho(z)$ and boundary conditions $\phi(z=0)=0$ and $\phi(z=L)=V_0$ is

$$\phi(z) = \frac{1}{\epsilon}\int_0^L \rho(\zeta)G(z|\zeta)d\zeta + \frac{V_0}{L}z, \tag{6}$$

where ϵ is the dielectric constant of the material, V_0 is applied bias voltage including the 1.5-V built-in voltage, and L is the total length of the intrinsic layer. The carrier density must be considered for both electrons and holes, along with their signs. After the calculation of the electric potential, the derivative gives the local electric field.

Third step: carrier velocities are given by the velocity-field curves described in Sec. V A with reference to the local electric field. We used velocity-field tables initially loaded from precalculated files to speed up the calculation. Then, the distance of the carriers' movement is calculated at each position in the MFSL. Obviously, the movements of the electrons and holes are different at each position owing to their different velocity-field curves.

After the movement, the carriers occupy new positions and then the new carrier density is decreased by radiative recombination. Since our selected time step of the calculation is far less than the time of the radiative recombination in the QW, the order of the calculation—i.e., the recombination calculation before or after the movement—does not affect the calculation results. We used a 1-ns lifetime of the radiative recombination, which is a typical value for GaAs QWs. Then, the calculation is looped to the first step. We note that we have not varied the radiative recombination lifetime with the local electric field and that we used a constant 1-ns value to speed up calculation time, since our calculation time for total applied bias voltages is considerable. Although the importance of considering the radiative recombination lifetime has been pointed out in previous reports,[2] for systems in this paper, the lifetime is thought to be less important. This is because, the radiative recombination lifetime of our MFSL systems estimated by overlap integral methods varies only within a factor of 10 or 100 for the various electric fields treated in this paper. On the other hand, the tunneling efficiencies of carriers through the TBs vary over tens of powers of 14 as shown in Fig. 8. Therefore, the influence of varying the radiative recombination lifetime is thought to be very small in our system. In contrast, conventional superlattices frequently have the same order of time between radiative recombination lifetime and tunneling time through the barriers separating QWs. In this case, influence of the recombination lifetime is thought to be important. However, the MFSL systems in this paper are not included in this system type. In addition, although we have done a simulation that applied variable radiative recombination lifetimes for local electric fields under a bias voltage where EFD formation arose, there have been no significant differences for EFD formation behavior. Therefore, the significance of the tunneling efficiency through the TB is dominant in the MFSL systems in this paper.

The calculation is continued until the electric-field distribution or the carrier distribution reaches a stationary state. We used a time step from 0.1 ps to 5 ps, since the time is also considerably less than the carrier drift time that corresponds to the time passing through a TB with the maximum carrier velocity under the highest electric field in the simulation. Regarding the following results, we used 5×10^5 loops with a 1-ps time step, which were needed to obtain a stationary condition. The reason for requiring such a large amount of time—i.e., 500 ns—to establish a stationary state is a result of the slow tunneling time through the TBs, which impedes completion of the final stationary state.

C. Simulation results

Figure 9 shows the calculated distributions of the electric potential and field under 9-V reverse-bias voltage and a 1-mW excitation condition, where the sample experimentally demonstrates the EFD as shown in Figs. 2(b) and 3(b). As shown, the electric field (dotted line) is separated into two domains—i.e., the LFD and HFD—at about 1500 ML. The FSLs' potential in the LFD is nearly flat, while there is a certain potential gradient for the TBs. In contrast, the electric field—i.e., the potential gradient—in the HFD is identical at both the FSL and TB regions. This result agrees well with our predicted model deduced from the experimental results (cf. Fig. 6).

Figure 10 shows the calculated domain boundary under various bias voltages with a 1-mW excitation. Note that a zero bias voltage corresponds to a 1.5-V total electric potential, since the *p-i-n* diode sample has a built-in voltage of 1.5 V. Under the low bias voltage exemplified by 0 V in the figure, the electric potential in FSLs is nearly flat, and thus,

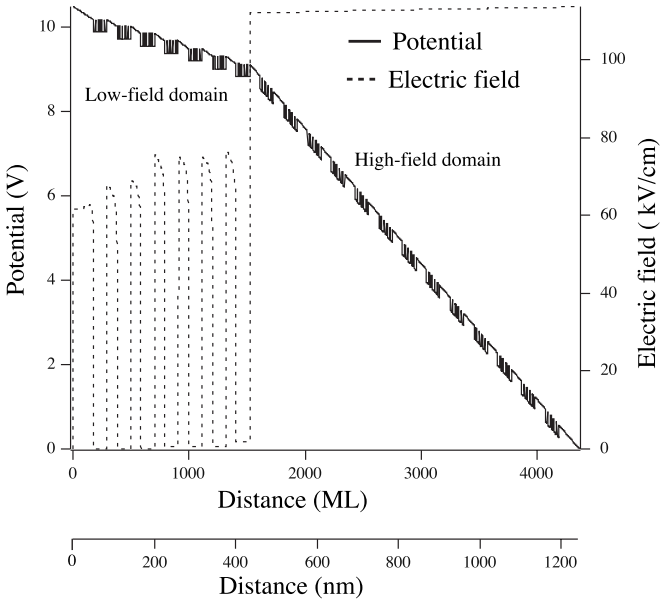

FIG. 9. Calculated distribution of electric field and electric potential at 9 V under 1-mW excitation. The potential curve is synthesized with the conduction band potential of the MFSL to clearly show the FSL and TB regions. Two bottom axes are shown. One is in monolayer (ML) units and the other is in nm units. The calculation was done using ML units.

the PL emission is from the miniband bottom, which agrees well with the experimental results. From the beginning of the EFD formation under a 2-V bias, the domain boundary advances toward the left side in the figure—i.e., the *p*-cap side—and finally diminishes at a 12-V bias. The reproduced phenomena in the simulation agree well with the tendency that appeared in the experimental results. However, this 12-V end voltage of the EFD formation is less than that in the experimental results, 15 V. We assume that this difference comes from some differences in constants in the simulation: e.g., the spot size of the excitation light, the absorption coefficient of the HeNe laser, etc.

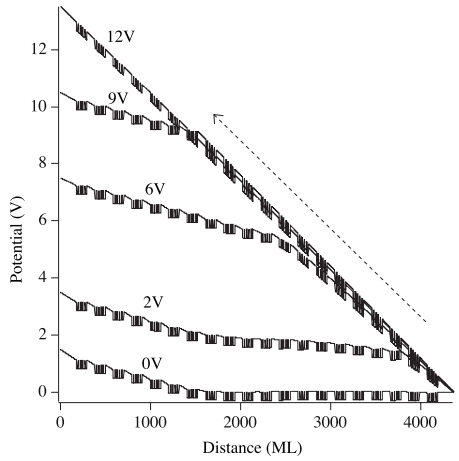

FIG. 10. Movement of domain boundary. The dashed arrow indicates the movement of the domain boundary while increasing the bias voltage. ML is monolayer units.

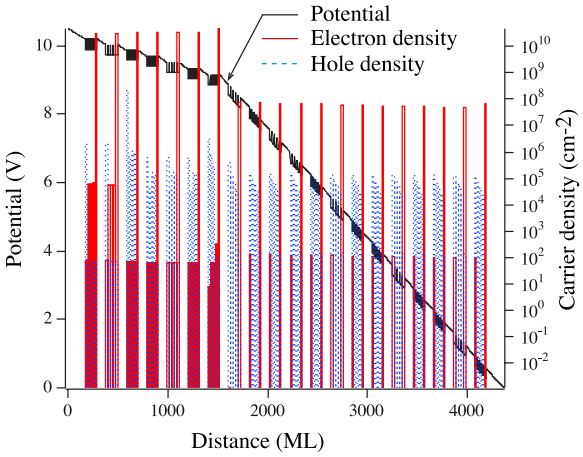

FIG. 11. (Color online) Calculated distribution of electric potential (solid line pointed by an arrow), electron density (solid line), and hole density (dotted line) under 9-V reverse-bias voltage. ML is monolayer units.

Under low bias voltage, Fig. 10 shows that many FSLs have a nearly flat potential. This creates a larger PL emission from the miniband's bottom and small emissions from the localized subbands in the HFD due to the quenching of PL by a fast carrier transport. This result agrees well with the experimental results shown in Figs. 3(b) and 5.

Figure 11 shows the calculated distributions of the electric potential and the density of electrons and holes, under a 9-V reverse-bias voltage and a 1-mW excitation condition. As predicted by the model in Fig. 6, electrons are gathered into the rightmost QW in each FSL, and the density is larger in the LFD than in HFD. In contrast, although the hole distribution is higher in the leftmost QWs in FSLs, the concentration is moderate, which is different from our predictions (cf. Fig. 6). However, the difference in carrier density for electrons and holes is sufficient to generate field screening. Therefore, this simulated distribution might be more plausible in a real MFSL system. Since the tunneling velocity in FSLs for holes is less than that for electrons under low electric fields, the holes might not gather as fast as the electrons.

Figure 12 shows the calculated *I-V* curve under a 1-mW excitation condition. Apparently, there are about 20 oscilla-

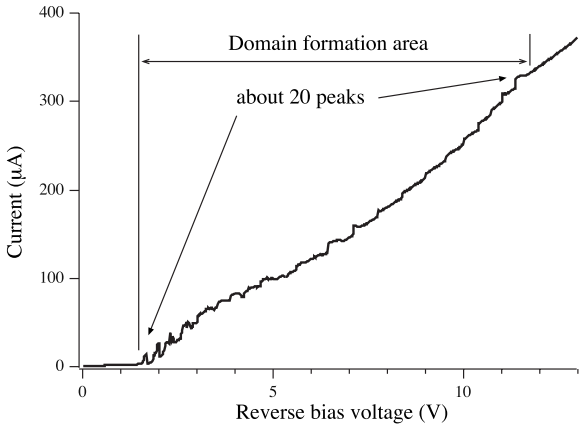

FIG. 12. Calculated *I-V* curve under 1-mW excitation.

tions in the photocurrent, which agrees well with the experimental result in Fig. 2(b). There is a small difference in voltage range where the EFD appears—i.e., 2–12 V in simulation and 1–15 V in experiments—which is thought to come from the differences in the constants we used: e.g., underestimation of absorption coefficient, etc. However, steplike oscillations in the *I-V* curve are clearly reproduced.

The origin of the steplike oscillation can be explained from the simulation results. During the movement of the domain boundary, the potential gradient in a FSL is rapidly changed from low to high; i.e., a LFD to HFD transition occurs within a short voltage interval due to the attraction effect in nonlinear phenomena. From our simulation, the transition voltage interval was 0.02 V. The output current, taking into account the displacement current, is given by the notation[17]

$$i = \frac{e}{L}\int_{x=0}^{L} \rho(x)v(x)dx, \tag{7}$$

where L, ρ, and v are length of the intrinsic layer in a *p-i-n* photodiode, carrier density, and carrier velocity, respectively. With the transition of the electric field in a FSL from low to high—i.e., affiliation transfer of a FSL from LFD to HFD—the number of FSLs, which have a large carrier velocity, increases. Since the carrier velocity in the HFD is greater than the LFD and the LFD-HFD transition occurs rapidly, increase of the output current is also abrupt, which is observed as a steplike increase in the *I-V* curve. As a result, this process clearly explains the origin of the oscillation in the experimental *I-V* curve. Note that since the increase in velocity overwhelms the decrease in carrier density, the product ρv increases after the transition from the LFD to the HFD.

D. Simulation results for low carrier density

Figure 13 shows the calculated *I-V* curve, electric potential, and spatial distribution of an electric field under a low excitation intensity—i.e., 10 μW. There is no fine-structure in the *I-V* curve, which indicates that an EFD is not formed. The almost straight potential curves under various reverse-bias voltages also show no sign of EFD formation. From the potential shape, we found that, all FSLs suffer from almost equivalent electric field. Distribution of the electric field in Fig. 13(c) also supports this conclusion. The field distribution indicates that the electric field in the TBs is greater than that in the FSLs under a low-bias-voltage region (V_b=5 V), which indicates slight concentration of the electric field in the TBs. In contrast, uniform field strength is applied in all areas of the MFSL under high bias voltage (V_b=12 V), since carrier transport efficiency through the TBs becomes sufficiently large to release carrier accumulation near the TBs. These results agree well with the experimental results under a low-excitation condition and the analysis in Sec. IV. However, spatial distribution of the electric field is not perfectly uniform at low voltages, as indicated by the dashed line under the 7-V curve in Fig. 13(b). From this fact, slight field screening exists even in 10-μW excitation. This supports the experimental result under 10-μW excitation shown in Fig. 3(a), the origin of the doublet in the −1 Stark-ladder PL, and the screening behavior of the Wannier-Stark localization in the experimental data.

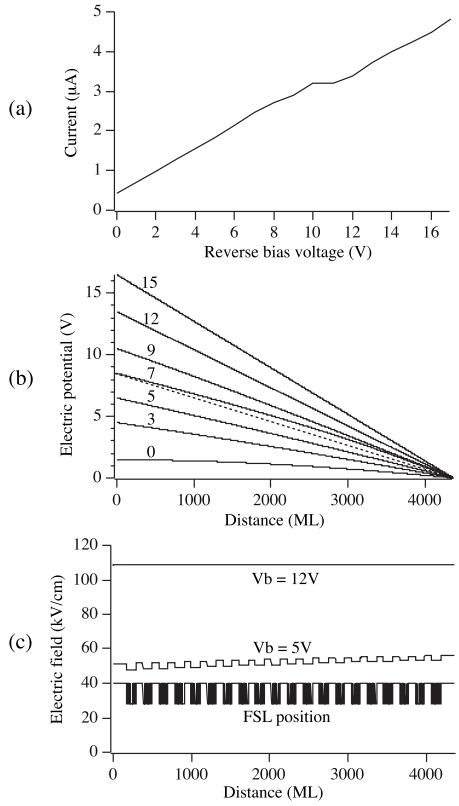

FIG. 13. Calculated results under 10-μW excitation. (a) *I-V* curve. (b) Electric potential under various reverse-bias voltages. Numbers on the curve indicate bias voltage (V). The dashed straight line is a guide for the eyes. The QW potential is not synthesized to the curves for clear display. ML is monolayer units. (c) Distribution of electric field under bias voltage Vb. "FSL position" indicates position of FSL and TB.

Regarding the slight oscillation of current at around 10 V in Fig. 13(a), we cannot explain it adequately, but we think that it might come from an accumulation of charges at the cladding layers at both ends in the sample structure, which modifies the output current from the finite multiple SLs. In Fig. 13(b), electric potential curves are convex under lower applied voltages than 12 V, but are straight from 12 V. This is thought to be because a slightly inhomogeneous electric field distribution is released from 12 V and a minute domain boundary reaches the cladding region.

VI. CONCLUSIONS

In summary, electric-field domain formation in a multiple finite-superlattice system was studied by experiment and numerical calculation. In this system, a particular electric-field domain was generated, which resulted from the difference in carrier transport velocity at the finite-superlattice and thick-barrier regions. Steplike current oscillation in the current-voltage characteristics was experimentally observed, which supported formation of electric-field domains. The distribution of the inner electric field was analyzed from the experi-

mental photoluminescence spectra, and a model of domain formation was proposed. Results from a numerical simulation agreed well with the experimental results and supported the model for the domain formation mechanism in multiple finite-superlattice systems.

ACKNOWLEDGMENTS

Part of this study was supported by a Grant-in-Aid (No. 18560013) from the Ministry of Education, Culture, Sports, Science, and Technology of Japan.

[1] L. Esaki and L. L. Chang, Phys. Rev. Lett. **33**, 495 (1974).
[2] *Semiconductor Superlattices*, edited by H. T. Grahn (World Scientific, Singapore, 1995), Chap. 5, and references therein.
[3] L. L. Bonilla and H. T. Grahn, Rep. Prog. Phys. **68**, 577 (2005), and references therein.
[4] E. E. Mendez, F. Agulló-Rueda, and J. M. Hong, Phys. Rev. Lett. **60**, 2426 (1988).
[5] J. Bleuse, G. Bastard, and P. Voisin, Phys. Rev. Lett. **60**, 220 (1988).
[6] K. H. Schmidt, N. Linder, G. H. Döhler, H. T. Grahn, K. Ploog, and H. Schneider, Phys. Rev. Lett. **72**, 2769 (1994).
[7] N. Linder, Phys. Rev. B **55**, 13664 (1997).
[8] A. M. Fox, D. A. B. Miller, G. Livescu, J. E. Cunningham, and W. Y. Jan, IEEE J. Quantum Electron. **27**, 2281 (1991).
[9] T. B. Norris, X. J. Song, W. J. Schaff, L. F. Eastman, G. Wicks, and G. A. Mourou, Appl. Phys. Lett. **54**, 60 (1989).
[10] S. M. Sze, *Physics of Semiconductor Devices*, 2nd ed. (John Wiley and Sons, New York, 1981), Chap. 9.2.
[11] C. Rauch, G. Strasser, K. Unterrainer, W. Boxleitner, E. Gornik, and A. Wacker, Phys. Rev. Lett. **81**, 3495 (1998).
[12] A. Sibille, J. F. Palmier, and F. Mollot, Appl. Phys. Lett. **60**, 457 (1992).
[13] F. Beltram, F. Capasso, D. L. Sivco, A. L. Hutchinson, Sung-Nee G. Chu, and A. Y. Cho, Phys. Rev. Lett. **64**, 3167 (1990).
[14] S. Adachi, J. Appl. Phys. **58**, R1 (1985).
[15] J. R. Haynes and W. Schockley, Phys. Rev. **81**, 835 (1951).
[16] J. D. Jackson, *Classical Electrodynamics*, 2nd ed. (John Wiley and Sons, New York, 1975), Chap. 1.
[17] A. Yariv, *Optical Electronics*, 3rd ed. (Holt-Saunders, New York, 1985), Chap. 10.4.